

# Manipulating surface states in topological insulator nanoribbons

Faxian Xiu<sup>1\*†</sup>, Liang He<sup>1†</sup>, Yong Wang<sup>1,2†</sup>, Lina Cheng<sup>2†</sup>, Li-Te Chang<sup>1</sup>, Murong Lang<sup>1</sup>, Guan Huang<sup>1</sup>, Xufeng Kou<sup>1</sup>, Yi Zhou<sup>1</sup>, Xiaowei Jiang<sup>1</sup>, Zhigang Chen<sup>2</sup>, Jin Zou<sup>2</sup>, Alexandros Shailos<sup>3</sup> and Kang L. Wang<sup>1\*</sup>

**Topological insulators display unique properties, such as the quantum spin Hall effect, because time-reversal symmetry allows charges and spins to propagate along the edge or surface of the topological insulator without scattering<sup>1–14</sup>. However, the direct manipulation of these edge/surface states is difficult because they are significantly outnumbered by bulk carriers<sup>9,15,16</sup>. Here, we report experimental evidence for the modulation of these surface states by using a gate voltage to control quantum oscillations in Bi<sub>2</sub>Te<sub>3</sub> nanoribbons. Surface conduction can be significantly enhanced by the gate voltage, with the mobility and Fermi velocity reaching values as high as  $\sim 5,800 \text{ cm}^2 \text{ V}^{-1} \text{ s}^{-1}$  and  $\sim 3.7 \times 10^5 \text{ m s}^{-1}$ , respectively, with up to  $\sim 51\%$  of the total conductance being due to the surface states. We also report the first observation of  $h/2e$  periodic oscillations, suggesting the presence of time-reversed paths with the same relative zero phase at the interference point<sup>16</sup>. The high surface conduction and ability to manipulate the surface states demonstrated here could lead to new applications in nanoelectronics and spintronics.**

Bi<sub>2</sub>Te<sub>3</sub> is well known as a thermoelectric material. It has also been predicted to be a three-dimensional topological insulator with robust and unique surface states consisting of a single Dirac cone at the  $\Gamma$  point<sup>3,11</sup>. Theorists have also predicted that it should be possible to observe a number of exotic particles (such as dyons, axions and majorana fermions) in topological insulators, suggesting a fertile field for the exploration of fundamental physics<sup>1,11,17</sup>. Angle-resolved photoemission spectroscopy (ARPES) experiments have now confirmed that the surface states of Bi<sub>2</sub>Te<sub>3</sub> have a single non-degenerate Dirac cone with a linear dispersion in momentum space<sup>18,19</sup>. Recent magnetotransport experiments in exfoliated Bi<sub>2</sub>Te<sub>3</sub> bulk materials have also suggested two-dimensional conduction channels originating from the surface states<sup>6</sup>. However, despite significant efforts in material doping<sup>18–20</sup> and electric gating<sup>9,15</sup>, it has been a challenge to modulate surface conduction because of the dominant bulk contribution due to impurities and thermal excitations in small-bandgap semiconductors<sup>6,9,21,22</sup>. With their large surface-to-volume ratios, topological insulator nanoribbons are expected to significantly enhance surface conduction<sup>22</sup>, and also enable surface manipulation by external means. Here, we have used thin Bi<sub>2</sub>Te<sub>3</sub> nanoribbons as conducting channels in field-effect transistor (FET) structures, and we demonstrate for the first time the possibility of surface state control in topological insulator nanostructures.

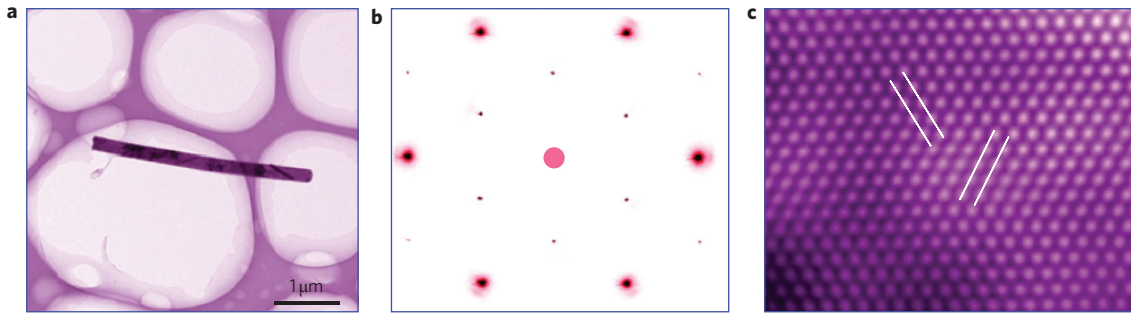
Transmission electron microscopy (TEM) was carried out to determine the structural characteristics of the Bi<sub>2</sub>Te<sub>3</sub> nanoribbons. Low-magnification TEM revealed a typical width of  $\sim 50$ – $230$  nm and

length in micrometres (Fig. 1a; Supplementary Fig. S1). Selected-area electron diffraction patterns revealed a perfect hexagonal structure with a single-crystalline rhombohedral phase (Fig. 1b). A typical high-resolution TEM image further confirmed the single crystallinity. The atomic plane spacings, marked by two pairs of parallel lines in Fig. 1c, were determined as  $0.22$  nm, which is consistent with those of the (11 $\bar{2}$ 0) atomic planes in Bi<sub>2</sub>Te<sub>3</sub> nanoplates<sup>23</sup>.

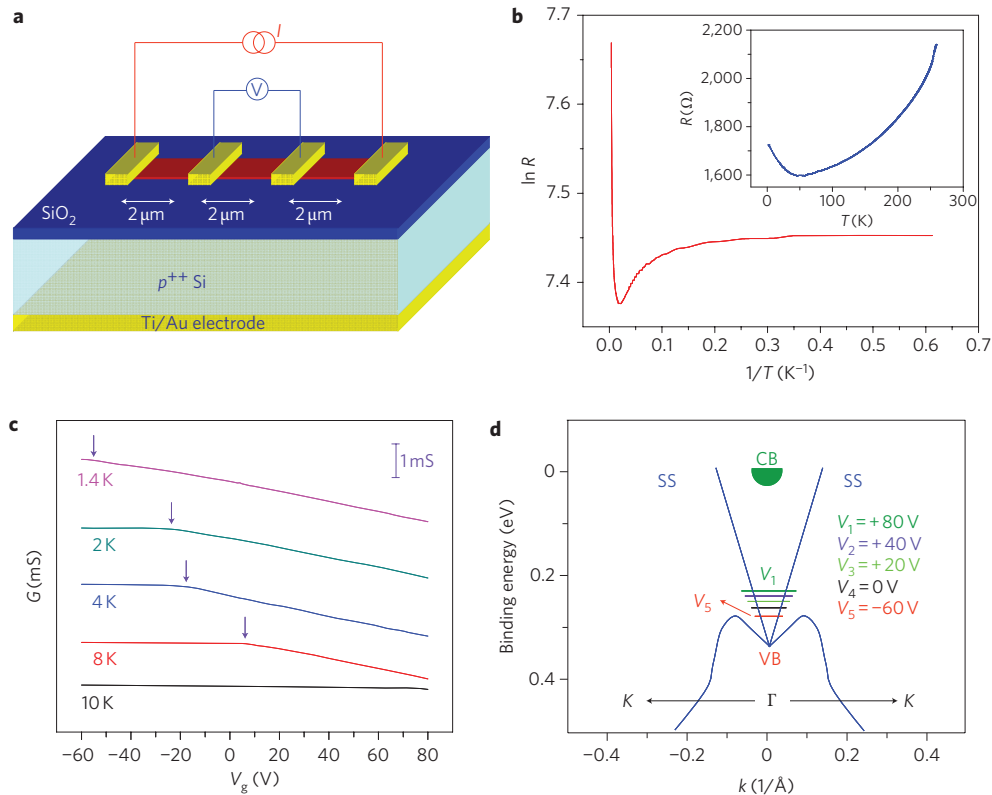
Back-gate FET devices with a standard four-terminal geometry were fabricated for transport measurements (shown schematically in Fig. 2a). The temperature dependence of the resistance is shown in Fig. 2b in linear (inset) and logarithmic scales. Channel resistance initially decreases with temperature, showing a typical metallic behaviour in the temperature range  $\sim 50$ – $300$  K (refs 6, 15, 24 and 25), in which phonon scattering dominates (Fig. 2b, inset). When the temperature drops below  $50$  K, the resistance increases, primarily due to the carrier freeze-out effect, similar to that observed in lightly doped Bi<sub>2</sub>Se<sub>3</sub> (ref. 25). We have attempted to extract the activation energy  $E_a$  in the temperature range  $\sim 20$ – $50$  K, where a nearly linear relation exists for  $R \approx e^{E_a/k_B T}$  (Fig. 2b, logarithmic scale), where  $R$  is the channel resistance,  $k_B$  is the Boltzmann constant, and  $T$  is the measurement temperature. Note that our fitting result yields only a small activation energy, less than  $1$  meV, which cannot be explained simply by the impurity levels in the Bi<sub>2</sub>Te<sub>3</sub> (refs 18 and 19). In this temperature range, surface conduction can be enhanced compared to that at higher temperatures, therefore becoming a non-negligible component. The multiple-channel conduction<sup>6</sup> makes the equation  $R \approx e^{E_a/k_B T}$  invalid for extracting the activation energy (see also the band diagram analysis in Supplementary Fig. S8). As will be discussed later, the surface conduction has approximately the same order of magnitude as bulk conduction in our nanoribbons. Further decreasing the temperature below  $20$  K does not lead to a significant change in resistance, as can be seen in the logarithmic plot (Fig. 2b). Although a clear  $R$ – $T$  plateau was not identified in a large temperature range, the small variation of resistance below  $4$  K (Fig. 2b, logarithmic plot) suggests the presence of surface conduction, which can be further supported by the observation of Shubnikov–de Haas (SdH) and Aharonov–Bohm (AB) oscillations<sup>6,22</sup>.

Figure 2c shows the channel conductance  $G$  as a function of both gate voltage  $V_g$  and  $T$ . Under zero gate bias, the total conduction at  $T \approx 1.4$ – $10$  K falls in the range  $\sim 6.3$ – $6.4$  mS. As the gate voltage increases, the conductance decreases, exhibiting a clear  $p$ -type semiconductor behaviour, which is in a good agreement with typical  $p$ -type characteristics from undoped Bi<sub>2</sub>Te<sub>3</sub> crystals<sup>6</sup>. It is believed that the general change in conductance as a function of gate bias suggests bulk hole conduction as the dominant component during

<sup>1</sup>Department of Electrical Engineering, University of California, Los Angeles, California 90095, USA, <sup>2</sup>Materials Engineering and Centre for Microscopy and Microanalysis, The University of Queensland, Brisbane, Queensland 4072, Australia, <sup>3</sup>California Nanosystems Institute, University of California, Los Angeles, California 90095, USA; <sup>†</sup>These authors contributed equally to this work. \*e-mail: xiu@ee.ucla.edu; wang@ee.ucla.edu



**Figure 1 | Structural characterizations of a  $\text{Bi}_2\text{Te}_3$  nanoribbon.** **a**, Low-magnification TEM image of a  $\text{Bi}_2\text{Te}_3$  nanoribbon on a holey carbon grid. The nanoribbon in this image is  $\sim 230$  nm wide and  $\sim 3.5$   $\mu\text{m}$  long. **b**, Selected area diffraction pattern taken along the  $\text{Bi}_2\text{Te}_3$  [0001] direction. Sharp diffraction spots indicate high-quality single crystals. **c**, High-resolution TEM image taken along the  $\text{Bi}_2\text{Te}_3$  [0001] direction, revealing a perfect crystalline structure. The spacing between the (11 $\bar{2}$ 0) atomic planes is measured to be 0.22 nm (marked by two pairs of parallel lines in **c**).



**Figure 2 | Electrical transport measurements of a nanoribbon FET.** **a**, Schematic of a typical back-gate FET device. The nanoribbon has a width of  $\sim 185$  nm, thickness of  $\sim 30$  nm and channel length of  $\sim 2$   $\mu\text{m}$ . A constant current geometry was used during transport measurements. **b**, Channel resistance  $R$  on a logarithmic scale versus the inverse of temperature,  $1/T$ . Inset:  $R$  versus  $T$ . **c**, Channel conductance  $G$  versus gate voltage  $V_g$  at five different temperatures; the magnetic field is zero. Arrows indicate a systematic shift of the Fermi level when applying gate biases at different temperatures. All curves are vertically shifted for clarification. **d**, Sketch of surface-state dispersion near the  $\Gamma$  point showing surface states (SS), valence band (VB) and conduction band (CB) of the bulk states (from refs. 6 and 18). The Fermi level (horizontal lines) shifts towards the middle of the bandgap as the gate voltage is increased from  $-60$  V to  $+80$  V, resulting in the bulk making a smaller contribution to the overall conduction of the system.

transport. Note that there are singularity points when the temperature falls to  $\sim 2$ – $8$  K (arrows in Fig. 2c), where the Fermi level is speculated to lift up from the valence band edge, leading to a sudden change in the  $G$ – $V_g$  slope. Figure 2d presents a sketch of the band structure and surface state dispersion near the  $\Gamma$  point. The Fermi levels indicated in this sketch are confirmed by the observed voltage-controlled SdH oscillations, as will be described below and are qualitatively consistent with the aforementioned  $G$ – $V_g$  plots.

One of the most intriguing challenges in topological insulators is identification of the surface states. Quantum oscillations such as

SdH and AB interference currently comprise the most convincing evidence of surface electronic states<sup>16,26</sup>. In parallel with the few experimental efforts regarding transport measurements<sup>6,24–27</sup>, we have carried out extensive investigations into voltage-controlled SdH oscillations and AB interference, aiming to understanding the controllability of the quantum behaviour of these surface states. In the following, we present dual evidence that both quantum oscillations can be enhanced when the bulk contribution is reduced by an external gate bias.

Magnetotransport measurements in a transverse device geometry were carried out at low temperatures. The magnetic field  $H$  is

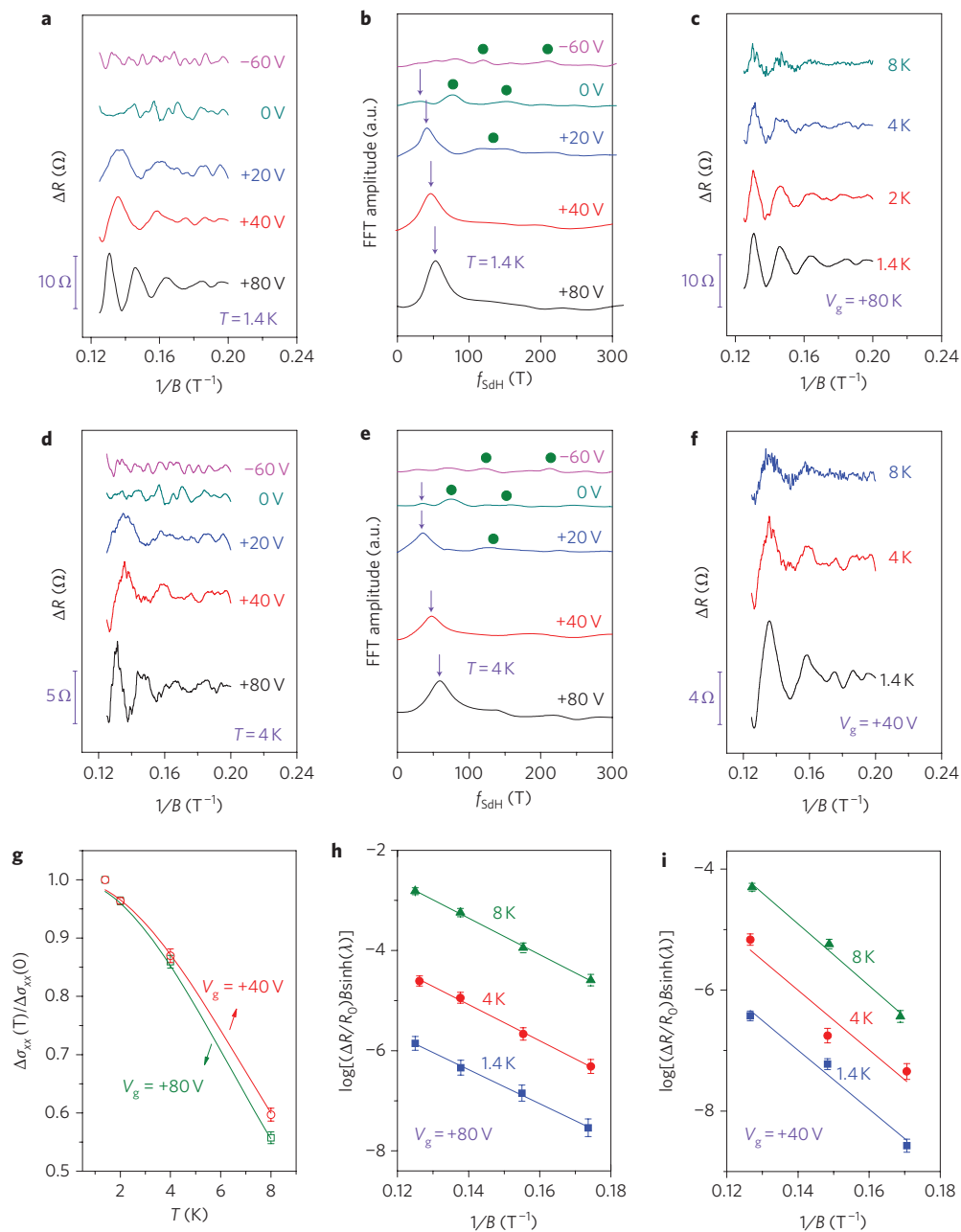


**Figure 3 | SdH oscillations in a nanoribbon FET.** **a–f**, Shubnikov-de Haas oscillations at different temperatures and gate voltages. The oscillations become more pronounced as the gate voltage increases from  $-60$  V to  $+80$  V at  $T = 1.4$  K (**a**) and  $4$  K (**d**). Purple arrows in the corresponding FFT spectra (**b,e**) indicate the frequency of the SdH oscillations, which represent the surface states. Green solid dots suggest the presence of other oscillation frequencies, which are developed when the bulk carrier concentration increases under negative gate voltages. The oscillations also become more pronounced as the temperature decreases from  $8$  K to  $1.4$  K at gate voltages of  $+80$  V (**c**) and  $+40$  V (**f**). **g**, Normalized conductivity amplitude versus temperature at gate voltages of  $+80$  V and  $+40$  V. A magnetic field of  $7.4$  T was used to extract the cyclotron effective mass:  $\sim 0.131m_0$  ( $+80$  V) and  $\sim 0.119m_0$  ( $+40$  V). **h,i**, Dingle plots at three different temperatures at gate voltages of  $+80$  V (**h**) and  $+40$  V (**i**). Transport lifetime, mean free path and mobility can be extracted from the best fit to  $\log[(\Delta R/R_0)B\sinh(\lambda)]$ .

perpendicular to both current flow and the nanoribbon surface. Under zero gate bias at  $1.4$  K, the magnetoresistance does not show an evident SdH oscillation (Fig. 3a, dark cyan); instead, the spectrum exhibits a nearly linear magnetoresistance with superimposed universal conductance fluctuations (UCFs; Supplementary Fig. S2b,c;  $V_g = 0$  V). By applying a positive gate voltage ( $20$ – $80$  V), however, the hole carriers in the bulk material are partially depleted, leading to reduced bulk conduction. The surface states in this scenario manifest themselves through progressively growing SdH oscillations, as shown in Fig. 3a. Correspondingly, fast

Fourier transform (FFT) spectra show dominant oscillation frequencies ( $f_{\text{SdH}}$  (T), Fig. 3b), in accordance with the SdH periodicities (Fig. 3a). We also note that the frequency peaks shift steadily towards higher magnetic fields, suggesting an increase in the two-dimensional carrier density of the surface. In contrast, a negative voltage on the gate induces holes into the bulk material, leading to diminished SdH oscillations and pronounced UCFs (Fig. 3a;  $V_g = -60$  V). To further verify the genuine nature of this controllability, we performed the same experiments at  $4$  K (Fig. 3d,e), where the oscillation amplitudes apparently decrease compared to those at

**Table 1 | Estimated parameters from the SdH oscillations at  $T = 1.4$  K.**

$V_g$ (V)	$f_{\text{SdH}}$ (T)	$n_{2\text{D}}$ ( $10^{12} \text{ cm}^{-2}$ )	$m_{\text{cycl}}$ ( $m_0$ )	$k_F$ ( $\text{\AA}^{-1}$ )	$V_F$ ( $10^5 \text{ ms}^{-1}$ )	$E_F$ (meV)	$T$ ( $10^{-13}$ s)	$\ell$ (nm)	$\mu$ ( $\text{cm}^2/\text{V}^{-1}\text{s}^{-1}$ )
+20	40.3	0.97	$0.111 \pm 0.002$	0.035	3.68	~85	—	—	—
+40	47.5	1.1	$0.119 \pm 0.003$	0.038	3.67	~92	~3.11	~114	~4,560
+80	58.1	1.4	$0.131 \pm 0.002$	0.042	3.74	~103	~4.28	~160	~5,790

1.4 K (Fig. 3a,b). It is well known that SdH oscillation is a characteristic of the two-dimensional Fermi surface<sup>6</sup>, where magnetoresistance varies periodically with the inverse of the magnetic field  $\Delta(1/B)$  through the following equations<sup>22,27</sup>:  $\Delta(1/B) = e/(hn_{2\text{D}})$  and  $\Delta(1/B) = 4\pi e/k_F^2 h$ , where  $B$  is magnetic flux density,  $n_{2\text{D}}$  is the two-dimensional carrier density,  $k_F$  is the Fermi vector,  $e$  is the electron charge, and  $h$  is Planck's constant. By using the obtained FFT peak values with  $V_g = +20$ ,  $+40$  and  $+80$  V (as shown in Fig. 3b,e),  $n_{2\text{D}}$  and  $k_F$  can be extracted. The calculated results are summarized in Table 1. Alternatively, these parameters can also be calculated based on the fitting of  $1/B$  versus the Landau level  $n$  (Supplementary Fig. S3).

The SdH amplitudes as a function of temperature were analysed to obtain more information about the surface states under constant voltages of  $+80$  and  $+40$  V (Fig. 3c,f, respectively). Oscillation amplitudes at both voltages decrease rapidly with a temperature increase from 1.4 to 8 K. The temperature-dependent amplitude  $\Delta\sigma_{\text{xx}}$  of the SdH oscillations is described by  $\Delta\sigma_{\text{xx}}(T)/\Delta\sigma_{\text{xx}}(0) = \lambda(T)/\sinh(\lambda(T))$  (ref. 6). The thermal factor is given by  $\lambda(T) = 2\pi^2 k_B T m_{\text{cycl}}/(\hbar e B)$  (refs 6 and 25), where  $m_{\text{cycl}}$  is cyclotron mass and  $\hbar$  is the reduced Planck constant. By taking the conductivity oscillation amplitude and performing the best fit to the  $\Delta\sigma_{\text{xx}}(T)/\Delta\sigma_{\text{xx}}(0)$  equation,  $m_{\text{cycl}}$  is extracted as  $\sim 0.131m_0$  at  $V_g = +80$  V and  $\sim 0.119m_0$  at  $V_g = +40$  V, as shown in Fig. 3g. Here,  $m_0$  is the electron rest mass. Because the cyclotron mass is given by  $m_{\text{cycl}} = E_F/V_F^2$  (ref. 6), where  $E_F$  and  $V_F$  are the Fermi level and Fermi velocity, respectively, both  $E_F$  and  $V_F$  can be precisely obtained provided  $m_{\text{cycl}}V_F = \hbar k_F$  (ref. 26). Note that the Fermi level moves from  $\sim 85$  meV towards the middle of the bandgap,  $\sim 103$  meV, when increasing the gate voltage from  $+20$  V to  $+80$  V (Table 1, Fig. 2d). The Fermi velocity, however, remains constant, saturating at  $\sim 3.7 \times 10^5 \text{ m s}^{-1}$ . This saturation behaviour can be explained by the linear dispersion relation of the surface states<sup>6,18</sup> (Fig. 2d) described by  $E_F = (\hbar V_F)k_F$ , where  $\hbar V_F$  is the slope of the energy  $E$  versus the vector  $k$  in momentum space. The systematic development of SdH oscillations under external gate biases clearly presents strong experimental evidence of the tunability of the surface states, which are, in essence, induced by shifting of the Fermi level (Table 1, Fig. 2d), together with partial depletion of bulk carriers.

We can also estimate the transport lifetime of the surface states ( $\tau$ ) by considering the Dingle factor  $e^{-D}$ , where  $D = 2\pi^2 E_F/(\tau e B V_F^2)$  (refs 6, 24 and 26). Note that  $\Delta R/R$  is proportional to  $[\lambda(T)/\sinh(\lambda(T))]e^{-D}$ , and the lifetime can be inferred from the slope in the logarithmic plot of  $\log[(\Delta R/R_0)B \sinh(\lambda(T))] \approx [2\pi^2 E_F/(\tau e V_F^2)] \times (1/B)$  (Fig. 3h,i). By using extracted cyclotron masses at  $V_g = +40$  and  $+80$  V, the surface state lifetime can be estimated to be  $\sim 3.1 \times 10^{-13}$  and  $\sim 4.3 \times 10^{-13}$  s, respectively.

Next we will acquire important parameters such as mean free path  $\ell = V_F \tau$  and the surface mobility<sup>6,24,25</sup>  $\mu = e\tau/m_{\text{cycl}} = e\ell/\hbar k_F$ . Our calculation yields estimated mean free paths of 114 and 160 nm, and mobilities of  $\sim 4,560$  and  $\sim 5,790 \text{ cm}^2 \text{ V}^{-1} \text{ s}^{-1}$ , for  $V_g = +40$  and  $+80$  V, respectively. Such a long mean free path and such a high mobility re-confirm the existence of surface states, which are also consistent with those reported in  $\text{Bi}_2\text{Te}_3$ ,  $\text{Bi}_2\text{Se}_3$  and  $\text{Bi}_{1-x}\text{Sb}_x$  bulk materials<sup>6,22,26</sup>. The rich information obtained from the gate-modulated and temperature-dependent SdH oscillations allows the possibility of estimating the percentage of total conduction that is surface conduction. Table 2 provides two

typical conditions under which the surface [ $G(\text{surface}) = (e^2/h)k_F \ell$ ] and bulk conductance [ $G(\text{total})$ ] are provided. It is found that surface conduction can be dramatically enhanced up to  $\sim 51\%$  under a gate voltage of  $+80$  V. Compared to their bulk counterpart, these  $\text{Bi}_2\text{Te}_3$  nanoribbons have great advantages, with their large surface-to-volume ratio being crucial to enabling voltage-controlled quantum oscillations as well as high surface conduction.

We next analyse AB oscillations in the  $\text{Bi}_2\text{Te}_3$  nanoribbons and explore possible voltage-controlled phase interference. An external magnetic field was applied along the length of the nanoribbon, parallel to the direction of the electric current; conduction carriers remain phase-coherent after completing closed trajectories. Indeed, our low-temperature magnetoresistance measurements along this direction provided periodic resistance oscillations, even without the gate voltage (Fig. 4a). After subtraction of the smooth background (Supplementary Fig. S4a), periodic AB oscillations could be clearly resolved with a period of  $\sim 0.75$  T, corresponding to a sample cross-sectional area of  $5.54 \times 10^{-15} \text{ m}^2$  (Fig. 4b; Supplementary Fig. S4b); this value is consistent with sample dimensions of  $\sim 185$  nm (width) and  $\sim 30$  nm (thickness), as determined by atomic force microscopy. When the temperature was raised to 8 K, the amplitude of the AB oscillation diminished rapidly (Fig. 4b), suggesting that the bulk contribution affects the carriers' trajectories, and phase coherence can be jeopardized by the increased phonon scattering at elevated temperatures<sup>22</sup>.

To explore the possibility of gate modulation on these AB oscillations, both positive and negative gate biases were applied, with the aim of tuning the Fermi level. As expected, a positive gate voltage induces pronounced AB oscillations, but a negative voltage diminishes quantum interference (Fig. 4c,d), reminiscent of the results observed for the SdH oscillations. The same trend was also confirmed at  $T = 2, 4$  and  $6$  K (Supplementary Fig. S4c-h). To understand the origin of these AB oscillations, a FFT was performed (plotted in Fig. 4e). The prominent  $h/e$  oscillation frequency indicates that the surface carriers travel the perimeter of the nanoribbon without confining themselves to the top and bottom surfaces. This behaviour is in agreement with the scenario for  $\text{Bi}_2\text{Se}_3$  nanoribbons<sup>22</sup>, where electrons propagate coherently through the side-walls to produce the quantum interference effect. The presence of the  $h/2e$  frequency, however, suggests that there is the possibility that carriers could propagate in complete circles, clockwise or anti-clockwise, all with the same relative zero phase at the point of interference, and thus being robust against averaging<sup>16,28</sup>. The FFT amplitude of the AB oscillations was also plotted as a function of temperature (Fig. 4f). The  $T^{-1/2}$  fit indicates the absence of inelastic phonon scattering<sup>22</sup>. The phase-coherent diffusion length is described by  $L_\phi = (\ell V_F \tau_\phi)^{1/2}$ , where  $\tau_\phi$  is the mean time between inelastic events ( $\tau_\phi \approx \hbar/k_B T$ , ref. 22). At  $V_g = +80$  V,  $L_\phi$  can be estimated to be  $\sim 0.57 \mu\text{m}$ . Such a long phase-coherent diffusion length

**Table 2 | Estimated surface conduction percentage with zero magnetic field and at  $T = 1.4$  K.**

$V_g$ (V)	$G(\text{surface})$ (mS)	$R(\text{total})$ ( $\Omega$ )	$R_{\text{sheet}}(\text{total})$ ( $\Omega \square^{-1}$ )	$G_{\text{sheet}}(\text{total})$ (mS)	$G(\text{surface})/G_{\text{sheet}}(\text{total})$
+40	1.68	1,911.3	176.8	5.66	~30%
+80	2.60	2,138.3	197.8	5.06	~51%

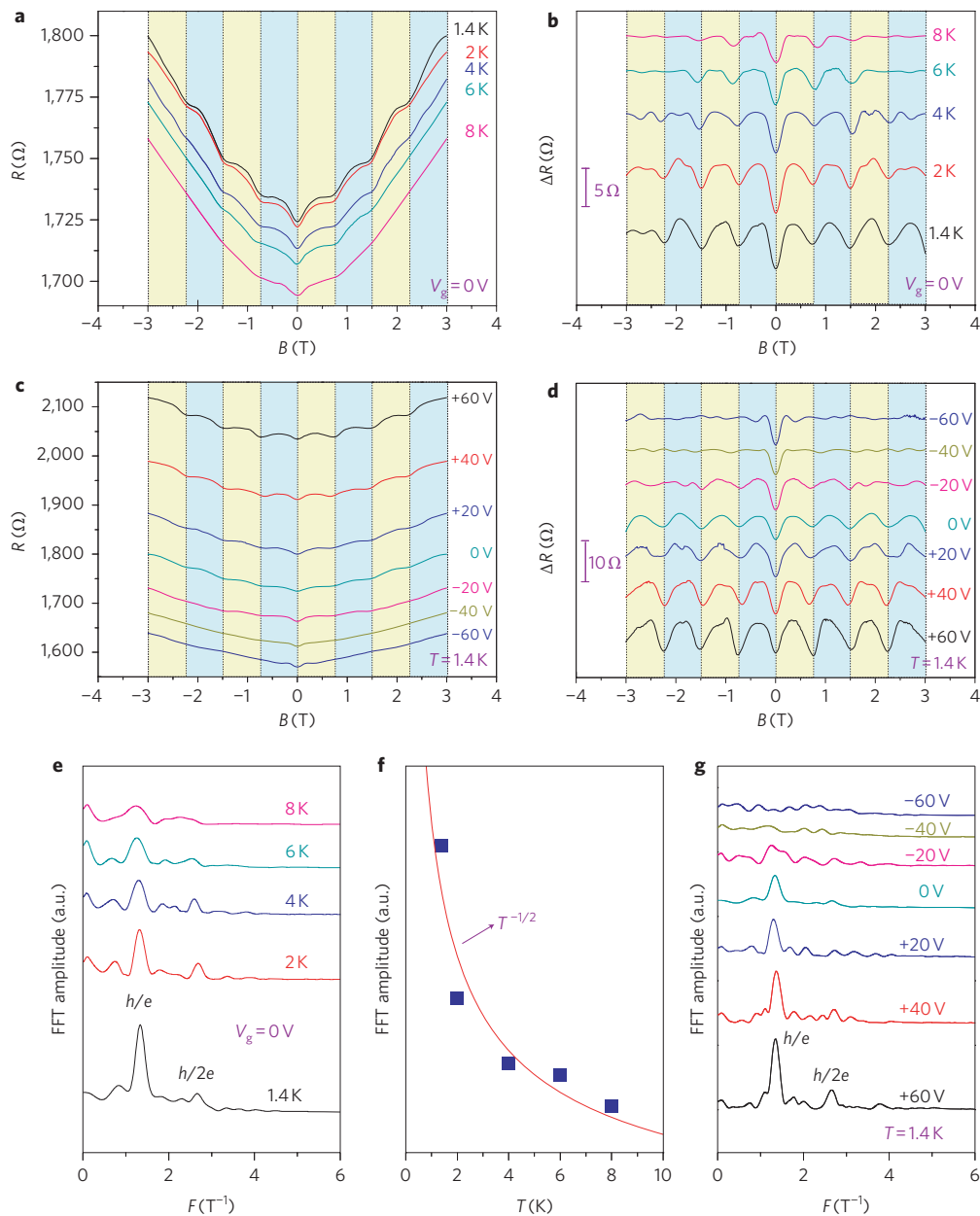


**Figure 4 | Gate-modulated AB oscillations.** **a**, Magnetoresistance plots (resistance  $R$  versus applied magnetic field  $B$ ) with superimposed Aharonov-Bohm oscillations at five different temperatures between 1.4 and 8 K, and no gate voltage. **b**, AB oscillations can be clearly seen when the smooth magnetoresistance background is subtracted from the plots in **a**. A detailed description of the subtraction method can be found in Supplementary Fig. S2a. **c**, Magnetoresistance plots at seven different gate voltages between  $-60$  and  $60$  V, at  $1.4$  K. **d**, Significant enhancement of the AB oscillation for positive gate voltages can be clearly seen when the smooth magnetoresistance background is subtracted from the plots in **c**. **e**, FFT of the magnetoresistance plots in **a** reveals AB oscillations with periods of  $h/e$  and  $h/2e$ , suggesting different interference paths during in-plane transport. The peaks at  $h/e$  and  $h/2e$  are most pronounced at  $1.4$  K. **f**, Amplitude of the FFT spectra in **e** versus temperature: the amplitude, fitted to  $T^{-1/2}$  (red line), suggests the absence of inelastic phonon scattering. **g**, AB oscillations with periods of  $h/e$  and  $h/2e$  can also be seen in the FFT of the magnetoresistance plots in **c**. The peaks at  $h/e$  and  $h/2e$  are most pronounced at a gate voltage of  $+60$  V.

would enable both  $h/e$  and  $h/2e$  oscillations, given the fact that the surface carriers could travel a long distance before randomly changing their wavefunction phase.

Finally, a FFT was also carried out for voltage-controlled AB interference at  $T = 1.4$  K (Fig. 4g). The dramatic development of the amplitude further verifies the tunability of phase interference on the surface using gate voltage. Both the voltage-controlled SdH and the AB oscillations suggest that by applying an external gate voltage, the Fermi level can be tuned away from the valence band, leading to the depressed

bulk conduction and the enhanced surface states. The successful modulation of the surface states in our study offers a ready pathway towards the practical applications of topological insulators.

### Methods

**Synthesis.** High-purity polyvinylpyrrolidone (PVP) was dissolved in ethylene glycol (36 ml), followed by the additions of  $\text{Bi}_2\text{O}_3$  powder (1 mmol), tellurium powder (3 mmol) and ethylenediamine tetraacetic acid (EDTA) powder. The resulting suspension was stirred vigorously and subsequently sealed in a steel autoclave. The autoclave was then heated to a temperature in the range  $180$ – $220$  °C and maintained

over 4 h. The synthesized products were collected by high-speed centrifugation, washed several times with distilled water and absolute ethanol, and finally dried at 50 °C for 48 h in an oven. Single-crystalline nanoribbons were formed during the synthesis process and were typically several micrometres in length and several hundreds of nanometres in width. The crystalline orientation of the as-grown nanoribbons was along [11 $\bar{2}$ 0] direction.

**Device fabrication and characterization.** Back-gate FET devices were fabricated by dispersing Bi<sub>2</sub>Te<sub>3</sub> nanoribbons on 300 nm SiO<sub>2</sub>/silicon substrates and subsequently using electron-beam lithography to fabricate electrodes (10 nm titanium and 90 nm gold). A typical FET device as used for the voltage-controlled experiments comprised a narrow Bi<sub>2</sub>Te<sub>3</sub> nanoribbon as a conducting channel, with a width of ~185 nm and a channel length of ~2 μm. Standard four-terminal electrodes were fabricated to eliminate contact resistance. A constant a.c. current of ~0.05–0.1 μA with a frequency of 130 Hz was fed through two outer contacts, and the voltage drop across inner pads was measured to determine resistance. The structural characteristics of the Bi<sub>2</sub>Te<sub>3</sub> nanoribbons were investigated using a FEI Tecnai F20 TEM. The bismuth/tellurium composition was analysed using an energy-dispersive spectroscopy technique. Transport measurements were carried out with a superconducting magnet system (American Magnetics). The lowest temperature used was 1.4 K, and the magnetic field could be up to ±8 T.

**AB interference.** It is widely considered that the AB interference of conductance is one of the most remarkable manifestations of electron phase coherence in mesoscopic samples. When two possible paths of an electron enclose magnetic flux, an observable interference effect occurs due to the phase difference,  $\Delta\phi_{AB}$ , between the two paths:  $\Delta\phi_{AB} = \oint e(S \cdot dl)/h = e\Phi/h = 2\pi\Phi/\phi_0$ . Here  $\Phi$  represents the magnetic flux enclosed by the paths,  $S$  is the cross-sectional area projected normal to the field, and  $\phi_0 = h/e$  is the flux quantum<sup>16,29</sup>. The topological insulator nanoribbons can be envisioned as hollow metallic cylinders with surface transport channels. The quantum interference of surface carriers with different paths in this hollow structure could make the conductance an oscillatory function of magnetic flux<sup>16,30</sup>.

Received 16 November 2010; accepted 21 January 2011;  
published online 13 February 2011

## References

- Hasan, M. Z. & Kane, C. L. Topological insulators. *Rev. Mod. Phys.* **82**, 3045–3067 (2010).
- Kane, C. L. & Mele, E. J. Topological order and the quantum spin Hall effect. *Phys. Rev. Lett.* **95**, 146802 (2005).
- Zhang, H. *et al.* Topological insulators in Bi<sub>2</sub>Se<sub>3</sub>, Bi<sub>2</sub>Te<sub>3</sub> and Sb<sub>2</sub>Te<sub>3</sub> with a single Dirac cone on the surface. *Nature Phys.* **5**, 438–442 (2009).
- Moore, J. Topological insulators: the next generation. *Nature Phys.* **5**, 378–380 (2009).
- Fu, L. & Kane, C. L. Topological insulators with inversion symmetry. *Phys. Rev. B* **76**, 045302 (2007).
- Qu, D.-X., Hor, Y. S., Xiong, J., Cava, R. J. & Ong, N. P. Quantum oscillations and Hall anomaly of surface states in the topological insulator Bi<sub>2</sub>Te<sub>3</sub>. *Science* **329**, 821–824 (2010).
- Xia, Y. *et al.* Observation of a large-gap topological-insulator class with a single Dirac cone on the surface. *Nature Phys.* **5**, 398–402 (2009).
- Zhang, T. *et al.* Experimental demonstration of topological surface states protected by time-reversal symmetry. *Phys. Rev. Lett.* **103**, 266803 (2009).
- Chen, J. *et al.* Gate-voltage control of chemical potential and weak antilocalization in Bi<sub>2</sub>Se<sub>3</sub>. *Phys. Rev. Lett.* **105**, 176602 (2010).
- Bernevig, B. A., Hughes, T. L. & Zhang, S.-C. Quantum spin Hall effect and topological phase transition in HgTe quantum wells. *Science* **314**, 1757–1761 (2006).
- Qi, X.-L. & Zhang, S.-C. The quantum spin Hall effect and topological insulators. *Phys. Today* **63**, 33–38 (January 2010).
- König, M. *et al.* Quantum spin Hall insulator state in HgTe quantum wells. *Science* **318**, 766–770 (2007).
- Ren, Z., Taskin, A. A., Sasaki, S., Segawa, K. & Ando, Y. Large bulk resistivity and surface quantum oscillations in the topological insulator Bi<sub>2</sub>Te<sub>3</sub>. *Phys. Rev. B* **82**, 241306 (2010).
- Zhang, Y. *et al.* Crossover of the three-dimensional topological insulator Bi<sub>2</sub>Se<sub>3</sub> to the two-dimensional limit. *Nature Phys.* **6**, 584–588 (2010).
- Checkelsky, J. G., Hor, Y. S., Cava, R. J. & Ong, N. P. Surface state conduction observed in voltage-tuned crystals of the topological insulator Bi<sub>2</sub>Se<sub>3</sub>. <http://arxiv.org/abs/1003.3883v1> (2010).
- Ihn, T. Topological insulators: oscillations in the ribbons. *Nature Mater.* **9**, 187–188 (2010).
- Fu, L. & Kane, C. L. Superconducting proximity effect and Majorana fermions at the surface of a topological insulator. *Phys. Rev. Lett.* **100**, 096407 (2008).
- Chen, Y. L. *et al.* Experimental realization of a three-dimensional topological insulator, Bi<sub>2</sub>Te<sub>3</sub>. *Science* **325**, 178–181 (2009).
- Hsieh, D. *et al.* A tunable topological insulator in the spin helical Dirac transport regime. *Nature* **460**, 1101–1105 (2009).
- Wang, Z. *et al.* Tuning carrier type and density in Bi<sub>2</sub>Se<sub>3</sub> by Ca-doping. *Appl. Phys. Lett.* **97**, 042112 (2010).
- Checkelsky, J. G. *et al.* Quantum interference in macroscopic crystals of nonmetallic Bi<sub>2</sub>Se<sub>3</sub>. *Phys. Rev. Lett.* **103**, 246601 (2009).
- Peng, H. *et al.* Aharonov–Bohm interference in topological insulator nanoribbons. *Nature Mater.* **9**, 225–229 (2009).
- Kong, D. S. *et al.* Few-layer nanoplates of Bi<sub>2</sub>Se<sub>3</sub> and Bi<sub>2</sub>Te<sub>3</sub> with highly tunable chemical potential. *Nano Lett.* **10**, 2245–2250 (2010).
- Eto, K., Ren, Z., Taskin, A. A., Segawa, K. & Ando, Y. Angular-dependent oscillations of the magnetoresistance in Bi<sub>2</sub>Se<sub>3</sub> due to the three-dimensional bulk Fermi surface. *Phys. Rev. B* **81**, 195309 (2010).
- Analytis, J. G. *et al.* Bulk Fermi surface coexistence with Dirac surface state in Bi<sub>2</sub>Se<sub>3</sub>: a comparison of photoemission and Shubnikov–de Haas measurements. *Phys. Rev. B* **81**, 205407 (2010).
- Taskin, A. A. & Ando, Y. Quantum oscillations in a topological insulator Bi<sub>1-x</sub>Sb<sub>x</sub>. *Phys. Rev. B* **80**, 085303 (2009).
- Mallinson, R. B., Rayne, J. A. & Ure, R. W. de Haas–van Alphen effect in n-type Bi<sub>2</sub>Te<sub>3</sub>. *Phys. Rev.* **175**, 1049–1056 (1968).
- Chandrasekhar, V., Rooks, M. J., Wind, S. & Prober, D. E. Observation of Aharonov–Bohm electron interference effects with periods  $h/e$  and  $h/2e$  in individual micron-size, normal-metal rings. *Phys. Rev. Lett.* **55**, 1610–1613 (1985).
- Aharonov, Y. & Bohm, D. Significance of electromagnetic potentials in the quantum theory. *Phys. Rev.* **115**, 485–491 (1959).
- Bardarson, J. H., Brouwer, P. W. & Moore, J. E. Aharonov–Bohm oscillations in disordered topological insulator nanowires. *Phys. Rev. Lett.* **105**, 156803 (2010).

## Acknowledgements

The authors thank the Focus Center Research Program–Center on Functional Engineered Nano Architectonics (FENA), Defense Advanced Research Projects Agency (DARPA) and the Australia Research Council (DP0984755, DP0985084) for their financial support. K.L.W. thanks Jeff Rogers (DARPA) and Betsy Weitzman (FENA). Y.W. thanks the Queensland International Fellowship. F.X. acknowledges helpful discussions with Siguang Ma, Yabin Fan and Pramey Upadhyaya (UCLA) and Wei Peng (UC Riverside).

## Author contributions

F.X. and L.H. designed and fabricated the devices. F.X., L.-T.C., M.L. and A.S. carried out the measurements. L.-N.C., Y.W., Z.G.C. and J.Z. synthesized the Bi<sub>2</sub>Te<sub>3</sub> nanoribbons and performed structural analysis. Y.W., G.H., X.K., X.J. and Y.Z. contributed to the measurements and analysis. K.W. supervised the research. F.X., Y.W., L.H., J.Z. and K.W. wrote the paper, with help from all other co-authors.

## Additional information

The authors declare no competing financial interests. Supplementary information accompanies this paper at [www.nature.com/naturenanotechnology](http://www.nature.com/naturenanotechnology). Reprints and permission information is available online at <http://npg.nature.com/reprintsandpermissions/>. Correspondence and requests for materials should be addressed to F.X. and K.L.W.